Article | Open Access

Micro Nano Science

Gao *et al. Micro Nano Sci.* **2026**, *1*, 10 **DOI:**10.20517/mns.2026.05

Highly dispersed PtCo supported on mesoporous carbon nanospheres for efficient hydrogenation of furfural to furfuryl alcohol

Beibei Gao[#], Yuqing Luo[#], Xinxin Yu, Lianjun Wang, Wan Jiang, Pengpeng Qiu[*], Wei Luo[*]

Keywords:
Sulfur anchoring, mesoporous carbon nanospheres, pt-based bimetallic alloy clusters, catalytic transfer hydrogenation, furfural, furfuryl alcohol

Citation: Gao, B.; Luo, Y.; Yu, X.; Wang, L.; Jiang, W.; Qiu, P.; Luo, W. Highly dispersed PtCo supported on mesoporous carbon nanospheres for efficient hydrogenation of furfural to furfuryl alcohol. *Micro Nano Sci.* **2026**, *1*, 10. https://dx.doi.org/10.20517/mns.2026.05

Received: 8 May 2026
First Decision: 29 May 2026
Revised: 5 Jun 2026
Accepted: 8 Jun 2026
Published: 26 Jun 2026

Academic Editor:
Lu Han
Copy Editor:
Shu-Yuan Duan
Production Editor:
Shu-Yuan Duan

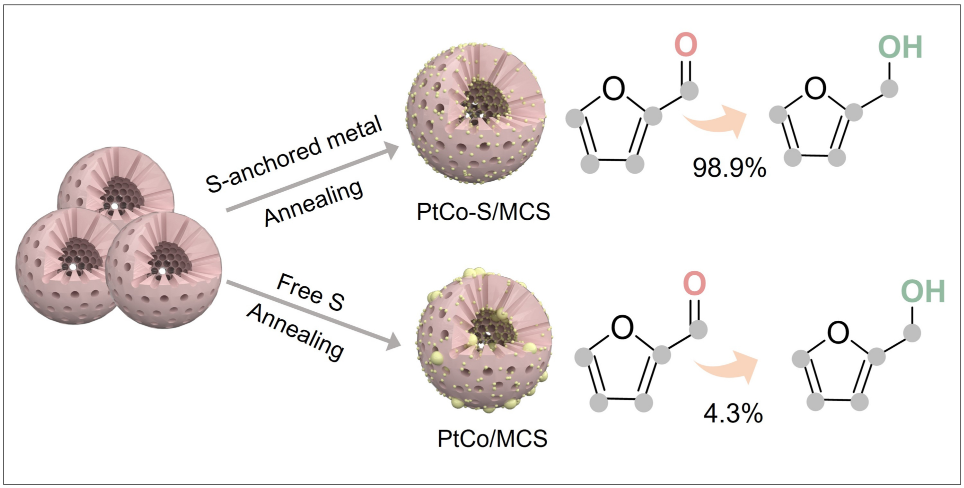

Abstract

Developing thermally stable bimetallic alloy clusters for furfural hydrogenation remains a significant challenge because high-temperature alloying readily causes metal migration and particle growth. In this study, ultrasmall Pt-based bimetallic clusters are constructed on a mesoporous carbon nanosphere (PtM-S/MCS) by combining a sulfur-anchored strategy to achieve efficient tandem conversion of furfural (FFA) into furfuryl alcohol (FOL). Characterization results show that the resultant materials possess a mesoporous carbon nanosphere (MCS) with a large specific surface area (1,482.8 m^2 g^{-1}) and uniform mesopores (≈ 7 nm), in which PtCo alloy clusters with a particle size of 2.1 nm are homogeneously dispersed. The strategy is further extended to PtFe-S/MCS and PtCu-S/MCS, demonstrating its applicability to different Pt-based bimetallic systems. In the selective hydrogenation of FFA, the PtCo-S/MCS catalyst achieves a 98.9% FOL yield. The enhanced performance arises from the cooperative effects of sulfur anchoring, mesoporous confinement, and PtCo alloy formation.

Check for updates

State Key Laboratory of Advanced Fiber Materials, College of Materials Science and Engineering, Donghua University, Shanghai 201620, China.
[#]These authors contributed equally to this work.

[*]**Correspondence to:** Dr. Pengpeng Qiu, Prof. Wei Luo, State Key Laboratory of Advanced Fiber Materials, College of Materials Science and Engineering, Donghua University, Shanghai 201620, China. E-mail: qiupengpeng@dhu.edu.cn; wluo@dhu.edu.cn

INTRODUCTION

The catalytic upgrading of biomass-derived platform molecules provides an important route toward sustainable production of fuels, polymers, and value-added chemicals. Among these intermediates, furfural (FFA) is particularly attractive because it can be readily obtained from hemicellulose-derived pentoses and further converted into a variety of furan-based chemicals[1-4]. Furfuryl alcohol (FOL), the selective hydrogenation product of furfural, is widely used in furan resins, foundry binders, polymer precursors, and fine chemicals[5,6]. Therefore, the efficient conversion of FFA to FOL represents a key transformation in biomass valorization and a representative reaction for studying the selective activation of carbonyl groups in multifunctional oxygenates.

Traditional FFA hydrogenation commonly relies on pressurized molecular hydrogen[7-9], which increases requirements for hydrogen handling, storage, and reactor safety. Catalytic transfer hydrogenation (CTH) offers a milder and operationally simpler alternative by using alcohols, especially isopropanol (IPA), as both solvent and hydrogen donor[10-13]. In this process, IPA is dehydrogenated to acetone while FFA is reduced to FOL through surface-mediated hydrogen transfer. However, achieving high activity and selectivity remains challenging. FFA contains both an aldehyde group and a furan ring, and its reaction network may involve competitive acetalization, condensation, ring hydrogenation, or over-reduction[14-16]. An efficient catalyst must therefore promote carbonyl activation and hydrogen transfer while suppressing undesired side reactions under liquid-phase conditions.

Pt-based catalysts are highly active for hydrogenation and transfer-hydrogenation reactions because of their strong ability to activate hydrogen species and their tunable electronic structures[17-19]. Alloying Pt with earth-abundant 3d transition metals, such as Co[20], Fe[21], or Cu[22], provides an effective strategy to regulate the adsorption and activation of oxygenated substrates. The secondary metal can modify the electronic structure of Pt, introduce oxophilic interfacial sites, and tune the binding configuration of furfural and reaction intermediates. These effects are particularly important for selective aldehyde hydrogenation, where balanced carbonyl adsorption and facile alcohol desorption are required. Nevertheless, Pt-based bimetallic catalysts often suffer from metal migration, particle coalescence, and compositional segregation during high-temperature alloying treatments[23,24]. These structural changes reduce metal utilization and weaken the interfacial effects that are essential for selective catalysis.

Constructing ultrasmall alloy clusters is a promising approach to maximize exposed active sites and strengthen metal-support interactions. Such clusters provide abundant low-coordination atoms and alloy interfaces that can facilitate both hydrogen-donor activation and carbonyl hydrogenation. However, the synthesis of ultrasmall alloy clusters remains difficult because the high-temperature annealing required for alloy formation also accelerates atomic diffusion and sintering[25]. Porous carbon supports offer high surface area, chemical stability, and mass-transport advantages, but they often lack sufficiently strong anchoring sites to immobilize metal precursors under thermal treatment[26,27]. A support-mediated strategy that simultaneously enables precursor confinement, alloy formation, and sintering resistance is therefore highly desirable.

Heteroatom anchoring provides a viable solution to this problem[28]. Among different heteroatoms, sulfur shows strong affinity toward noble and transition-metal species, allowing the formation of metal-sulfur coordination motifs that can immobilize metal precursors and regulate nucleation during annealing[27,29]. When incorporated into a mesoporous carbon framework, sulfur-containing groups may act as interfacial anchoring sites to restrict metal migration, stabilize small alloy domains, and modulate the local electronic environment of metal centers. However, sulfur incorporation must be carefully controlled, as excessive or poorly positioned sulfur species may block active sites. A rational sulfur-anchored architecture should therefore stabilize alloy clusters without sacrificing accessibility of the active metal surface.

Herein, we report a sulfur-anchored mesoporous carbon nanosphere strategy for constructing Pt-based bimetallic alloy catalysts. Mesoporous carbon nanospheres (MCS) were chosen as the support because their high surface area, interconnected mesopores, and robust spherical morphology provide an ideal platform for precursor infiltration, spatial confinement, and reactant diffusion. Sodium thioglycolate was introduced as a sulfur-containing ligand to coordinate Pt precursors and generate sulfur-mediated anchoring sites within the carbon framework. After incipient wetness impregnation and high-temperature reductive annealing, ultrasmall PtCo alloy clusters were uniformly confined in the MCS, whereas the sulfur-free counterpart formed larger, compositionally less uniform nanoparticles. The generality of this approach was further demonstrated with PtFe-S/MCS and PtCu-S/MCS. When applied to the CTH of FFA with IPA, PtCo-S/MCS exhibited 98.9% yield of FOL. Structural characterizations and catalytic studies reveal that the enhanced performance originates from the cooperative effects of mesoporous confinement, sulfur-mediated stabilization, and PtCo alloy formation. This work provides an interfacial anchoring strategy for designing thermally stable bimetallic nanocatalysts and offers insights into catalyst regulation for selective biomass upgrading.

EXPERIMENTAL

Synthesis of mesoporous carbon nanospheres

3.7 mL of NH_4OH (28-30 wt.%), 70 mL of ethanol, and 12 mL of deionized water were combined and stirred at room temperature for 10 min to form a homogeneous mixture. Subsequently, 0.4 g of resorcinol and 0.5 mL of formaldehyde (37 wt.%) were introduced, and the mixture was stirred for an additional 40 min to ensure complete dissolution and pre-polymerization. Thereafter, 3 mL of tetrapropoxysilane (TPOS) was added dropwise to initiate the co-condensation reaction at room temperature. After 12 h of reaction, the resulting solid product was collected by centrifugation and washed alternately with deionized water and ethanol at least three times to remove residual reactants. The obtained resorcinol-formaldehyde/silica (RF/SiO_2) composite nanospheres were subsequently carbonized at 800 °C for 2 h under an N_2 atmosphere with a heating rate of 3 °C min^{-1}. The silica template was then etched by immersion in 10% hydrofluoric solution for 12 h, followed by thorough washing with deionized water and ethanol (at least three times each) and drying at 60 °C overnight to obtain MCS, as illustrated in Figure 1.

Synthesis of MCS-supported sulfur-anchored metal catalysts (M-S/MCS)

The water uptake capacity of MCS was determined to be 4.27 mL g^{-1} prior to impregnation.

PtCo-S/MCS: 22 mg of H_2PtCl_6 and 6.7 mg of sodium thioglycolate (STG) were dissolved in 640 μL of deionized water and stirred at room temperature for 4-8 h. During this period, the Pt species were evidenced by a visible color change in the solution from yellow to orange-yellow, indicating successful Pt-thiolate complex formation. Subsequently, 33.6 mg of $CoCl_2 \cdot 6H_2O$ was added to the above solution and stirred for 15 min to obtain a homogeneous metal precursor solution. The precursor solution was then introduced into 150 mg of MCS via incipient wetness impregnation to ensure complete and uniform infiltration into the mesoporous carbon framework. After aging at room temperature for 6 h, the impregnated sample was transferred to a tube furnace and subjected to a two-stage thermal treatment under a H_2/Ar atmosphere: first at 900 °C for 2 h, then at 600 °C for 6 h, with a heating rate of 10 °C min^{-1}, to yield the PtCo-S/MCS catalyst, as illustrated in Figure 1.

PtFe-S/MCS: The synthesis procedure followed that of PtCo-S/MCS, with the exception that $CoCl_2 \cdot 6H_2O$ (33.6 mg) was replaced by $FeCl_3$ (24 mg). The thermal treatment was adjusted to 900 °C for 2 h, followed by 700 °C for 6 h under a H_2/Ar atmosphere at a heating rate of 10 °C min^{-1}, yielding the PtFe-S/MCS catalyst.

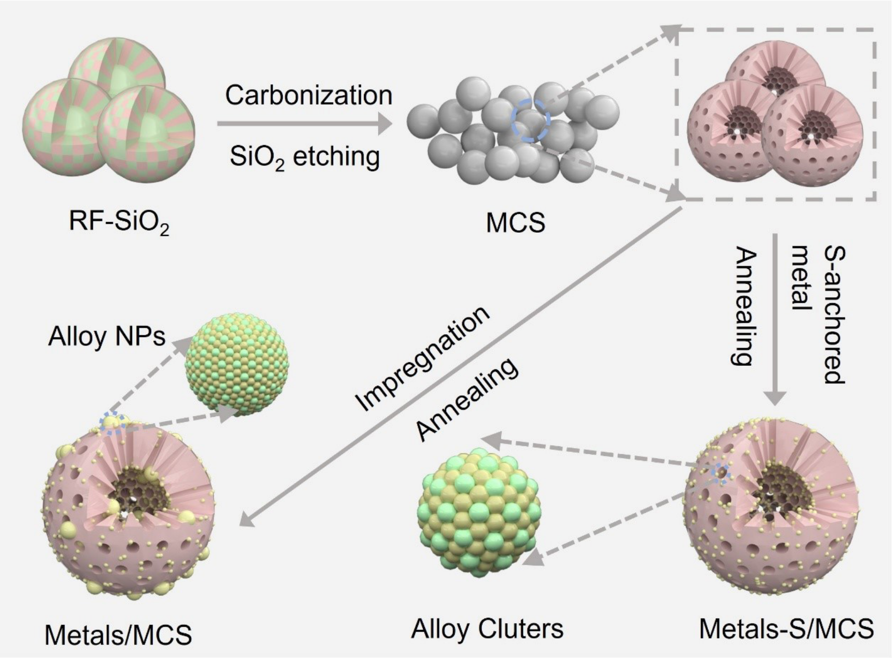

Figure 1. Schematic illustration of the synthesis procedure for MCS-supported sulfur-anchored bimetallic cluster catalysts (Metals-S/MCS) and the corresponding alloy nanoparticle counterparts (Metals/MCS). MCS: Mesoporous carbon nanospheres; RF: resorcinol-formaldehyde.

PtCu-S/MCS: The synthesis procedure followed that of PtCo-S/MCS, with the exception that $CoCl_2·6H_2O$ (33.6 mg) was replaced by $Cu(NO_3)_2·3H_2O$ (38.6 mg). The thermal treatment was adjusted to 800 °C for 2 h followed by 600 °C for 6 h under a H_2/Ar atmosphere at a heating rate of 10 °C min^{-1}, yielding the PtCu-S/MCS catalyst.

Synthesis of PtCo/MCS

For comparison, a reference catalyst without sulfur anchoring was prepared following a similar procedure. Specifically, for PtCo/MCS: 22 mg of chloroplatinic acid (H_2PtCl_6) and 33.6 mg of $CoCl_2·6H_2O$ were dissolved in 640 μL of deionized water and stirred at room temperature for 15 min to obtain a homogeneous metal precursor solution. The precursor solution was then introduced into 150 mg of MCS via incipient wetness impregnation. After aging at room temperature for 6 h, the impregnated sample was subjected to two-stage thermal treatment under an H_2/Ar atmosphere at 900 °C for 2 h, followed by 600 °C for 6 h, with a heating rate of 10 °C min^{-1}, yielding the PtCo/MCS catalyst, as illustrated in Figure 1.

Synthesis of PtCo-S/MCS

Twenty-two mg of H_2PtCl_6 and 33.6 mg of $CoCl_2·6H_2O$ were dissolved in 640 μL of deionized water and stirred at room temperature for 10 min. The precursor solution was then introduced into 150 mg of MCS via incipient wetness impregnation to ensure complete and uniform infiltration into the mesoporous carbon framework. After aging at room temperature for 6 h, the sample was transferred to a tubular furnace and calcined at 900 °C for 2 h under a H_2/Ar atmosphere to ensure complete alloying of Pt and Co. After cooling to room temperature, the obtained powder was placed downstream in a tubular furnace under an Ar atmosphere, while a porcelain boat loaded with thiourea was positioned upstream. The sample was subsequently heated at 350 °C for 2 h to introduce sulfur species, yielding the final PtCo/S/MCS catalyst.

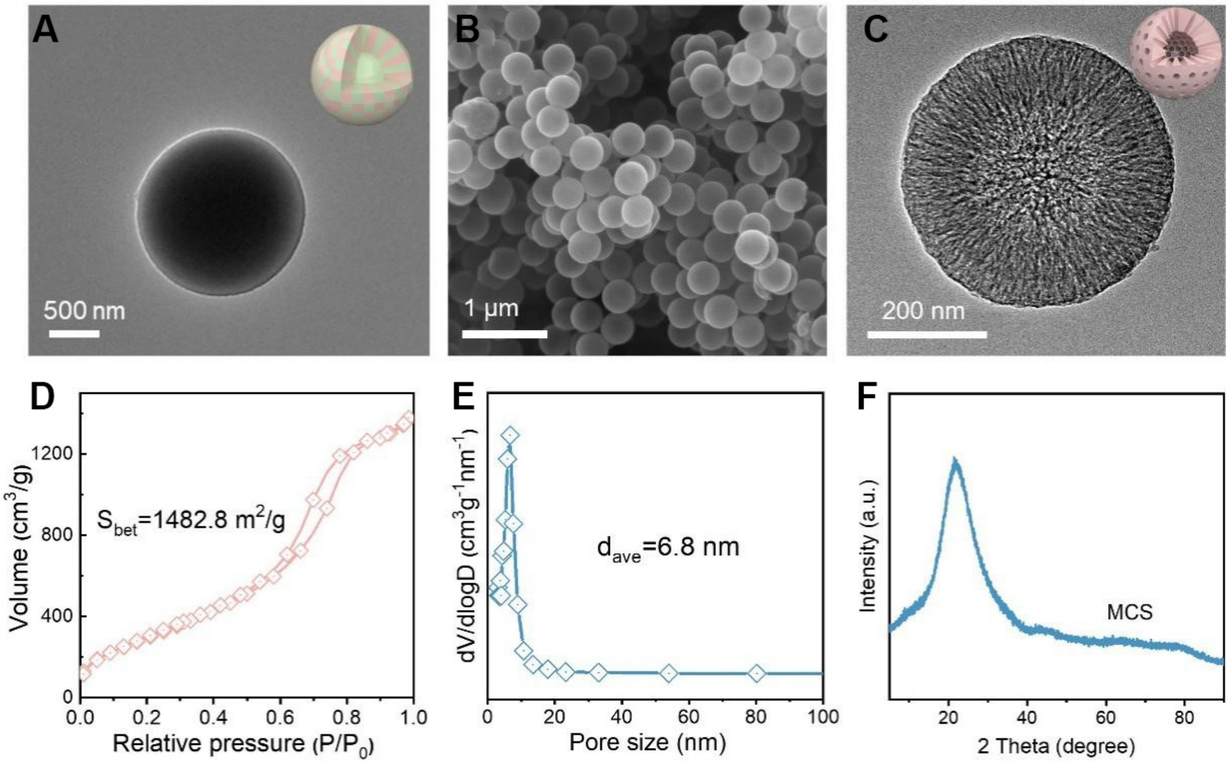

Figure 2. Structural and morphological characterization of MCS. (A) TEM image of RF-SiO_2 composite nanospheres. (B) SEM image; (C) TEM image; (D) N_2 adsorption-desorption isotherm; (E) pore size distribution curve; (F) XRD pattern of MCS. MCS: Mesoporous carbon nanospheres; RF: resorcinol-formaldehyde; SEM: scanning electron microscopy; TEM: transmission electron microscopy; XRD: X-ray diffraction.

RESULTS AND DISCUSSION

Structural and morphological characterization

The morphology and porous structure of the as-synthesized MCS were systematically characterized. As shown in Figure 2A, the transmission electron microscopy (TEM) image of the RF-SiO_2 precursor reveals smooth, solid spherical particles, confirming the successful co-condensation of the resorcinol-formaldehyde resin and silica components. Following carbonization at 800 °C and subsequent HF etching to remove the SiO_2 template, the resulting MCS retained its spherical morphology with a uniform size distribution, as evidenced by the SEM image in Figure 2B. The TEM image in Figure 2C further reveals a highly developed mesoporous interior structure within the carbon nanospheres, consistent with the removal of the silica framework and the formation of an interconnected pore network. N_2 adsorption-desorption measurements were performed to quantitatively assess the mesoporous characteristics of MCS. As shown in Figure 2D, the isotherm exhibits a typical Type IV profile with a distinct H_2-type hysteresis loop at relative pressures of 0.4-0.9, characteristic of mesoporous materials with ink-bottle-shaped pores[30], yielding a BET specific surface area of 1,482.8 m^2 g^{-1}. The corresponding pore size distribution derived from the desorption branch using the Barrett-Joyner-Halenda method [Figure 2E] shows a narrow distribution centered at approximately 6.8 nm, further confirming the uniform mesoporous architecture of MCS. Such a high surface area and well-defined mesoporosity are expected to facilitate metal precursor infiltration during impregnation and provide abundant accessible active sites for catalytic reactions. The X-ray diffraction (XRD) pattern of MCS [Figure 2F] displays two broad diffraction peaks centered at approximately 24° and 43°[31], indicative of the amorphous carbon nature of MCS with a low degree of graphitization.

Systematic characterizations were performed to elucidate the morphology and structure of MCS-supported Pt-based bimetallic catalysts. As shown in Figure 3A, the (111) diffraction peak of PtCo-S/MCS lies between

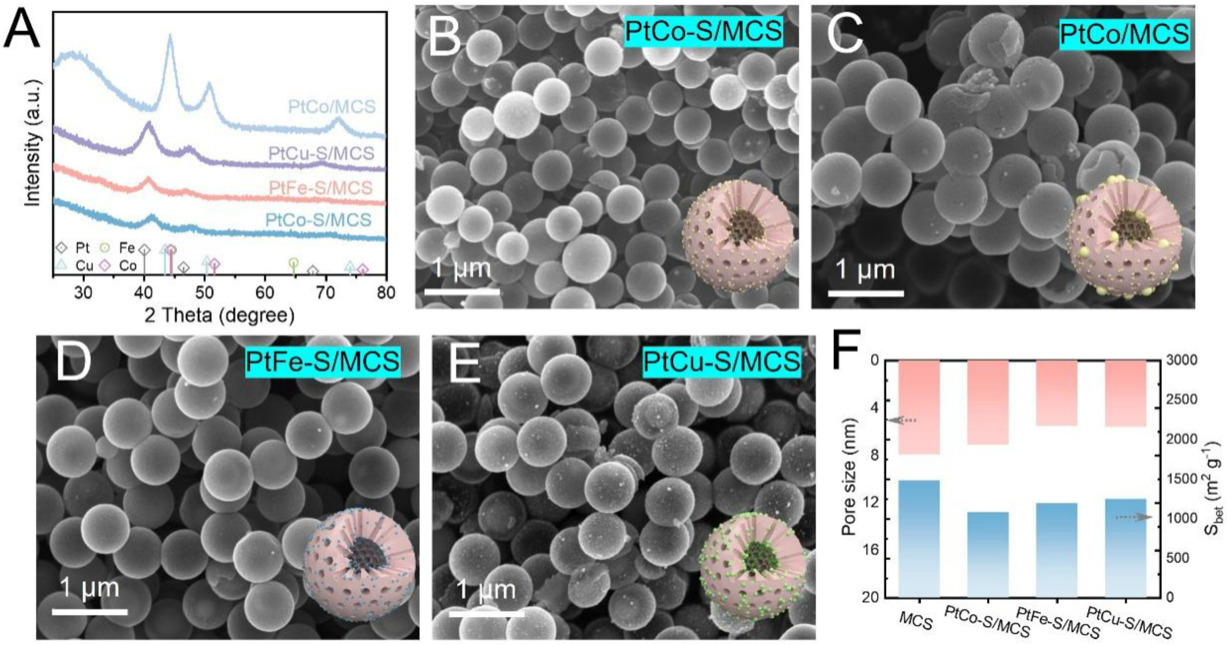

Figure 3. Structural characterization of the as-prepared Pt-based bimetallic catalysts. (A) XRD patterns and (B-E) SEM images of of PtCo-S/MCS, PtFe-S/MCS, PtCu-S/MCS, and PtCo/MCS catalysts;(F) Comparison of pore size and BET specific surface area of MCS, PtCo-S/MCS, PtFe-S/MCS, and PtCu-S/MCS. MCS: mesoporous carbon nanospheres; XRD: X-ray diffraction; SEM: scanning electron microscopy; BET: Brunauer-Emmett-Teller.

those of metallic Pt (PDF#001-1194, 40.0°) and Co (PDF#001-1255, 44.4°), supporting the formation of a PtCo alloy phase[32]. By contrast, the corresponding peak of sulfur-free PtCo/MCS is located closer to metallic Co, implying the formation of Co-rich alloy domains with less pronounced Pt incorporation. Similar peak shifts are also observed for PtFe-S/MCS and PtCu-S/MCS, supporting the formation of PtFe and PtCu alloy structures, respectively. No obvious diffraction peaks corresponding to isolated Co, Fe, Cu, or their oxide phases are detected, indicating that the secondary metals are mainly incorporated into Pt-based alloy domains. The broad diffraction profiles further suggest the nanosized nature of the alloy species, consistent with the confinement effect of the mesoporous carbon framework.

Scanning electron microscopy (SEM) images show that PtCo-S/MCS and PtCo/MCS retain the uniform spherical morphology of the MCS support after metal loading and high-temperature annealing [Figure 3B and C], confirming the structural robustness of the carbon nanospheres. Similar morphologies are observed for PtFe-S/MCS and PtCu-S/MCS [Figure 3D and E], indicating the versatility of the sulfur-anchored impregnation strategy across different Pt-based bimetallic catalysts. Furthermore, the incorporation of bimetallic alloy clusters into MCS reduces both pore size and BET specific surface area compared to pristine MCS [Figure 3F], which is attributed to the partial occupation of mesopores by the impregnated metal species. Nevertheless, all catalyst samples retain substantial surface areas and well-developed mesoporous structures, ensuring adequate exposure of the alloy active sites and efficient mass transport of reactants during catalytic reactions.

To further probe the internal structure of the catalysts, TEM characterization was performed. PtCo-S/MCS preserves the spherical mesoporous architecture of MCS, with ultrasmall metal clusters uniformly distributed throughout the carbon framework [Figure 4A and B]. The corresponding size distribution gives an average cluster diameter of 2.1 ± 0.5 nm, indicating that sulfur anchoring effectively suppresses metal migration and sintering during high-temperature annealing. The high resolution transmission electron microscopy

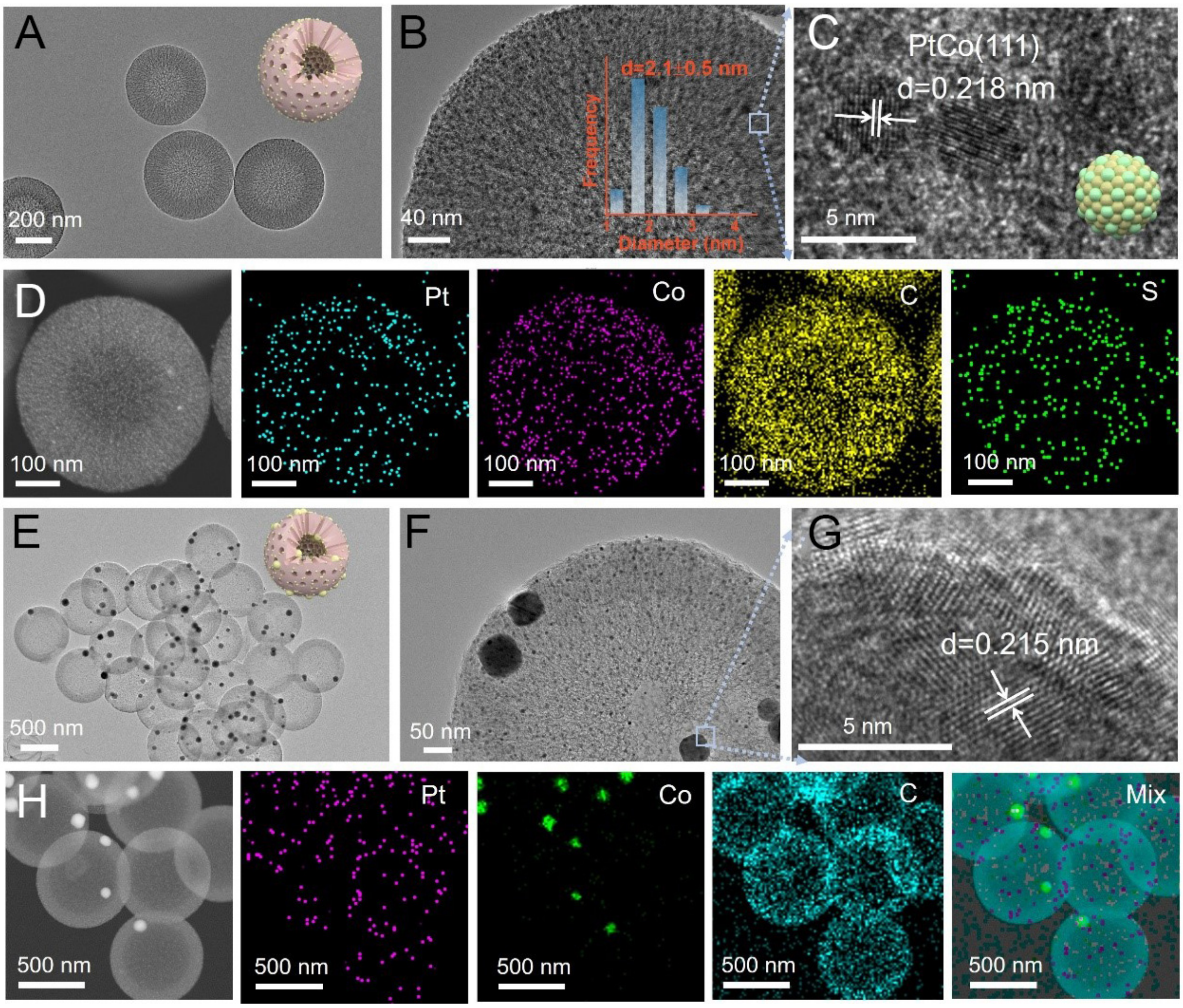

Figure 4. Microscopic characterization of PtCo–S/MCS and PtCo/MCS. (A and B) TEM images with the inset showing the size distribution of metal clusters; and (C) HRTEM image; (D) HAADF-STEM image and the corresponding EDS elemental mappings of PtCo–S/MCS; (E and F) TEM images; and (G) HRTEM image; (H) HAADF-STEM image and the corresponding EDS elemental mappings of PtCo/MCS. HRTEM: High resolution transmission electron microscopy; HAADF-STEM: high-angle annular dark-field scanning transmission electron microscopy; MCS: mesoporous carbon nanospheres; EDS: energy-dispersive X-ray spectroscopy; TEM: transmission electron microscopy.

(HRTEM) image [Figure 4C] reveals a lattice spacing of 0.218 nm, assignable to the PtCo (111) plane[33,34], further supporting the alloy structure indicated by XRD. High-angle annular dark-field scanning transmission electron microscopy (HAADF-STEM) and energy-dispersive X-ray spectroscopy (EDS) mappings [Figure 4D] further show homogeneous Pt and Co distributions with clear spatial co-localization, together with dispersed S species across the carbon nanosphere, supporting the formation of sulfur-stabilized PtCo alloy clusters. In contrast, PtCo/MCS prepared without sulfur anchoring exhibits pronounced metal aggregation, with large nanoparticles scattered across and inside the carbon nanospheres [Figure 4E and F]. Although the lattice spacing of 0.215 nm can also be indexed to the PtCo (111) plane[35], the larger particle size and less uniform elemental distribution indicate insufficient control over metal nucleation and growth in the absence of sulfur-mediated stabilization [Figure 4G]. The EDS mapping of PtCo/MCS [Figure 4H] shows a markedly inhomogeneous distribution of Pt and Co, with Co-rich domains associated with the larger particles, highlighting the compositional heterogeneity caused by uncontrolled sintering.

These results establish sulfur anchoring as a key structural regulator for confining PtCo alloy clusters within the mesoporous carbon framework. Rather than merely promoting alloy formation, the sulfur species primarily govern the dispersion, size confinement, and compositional uniformity of the bimetallic domains under reductive thermal treatment.

The generality of the sulfur-anchored strategy was further verified with PtFe-S/MCS and PtCu-S/MCS. PtFe-S/MCS preserves the spherical mesoporous architecture of MCS after high-temperature annealing, with ultrasmall metal clusters uniformly confined within the carbon framework [Figure 5A and B]. The narrow size distribution centered at 2.1 ± 0.6 nm indicates efficient suppression of metal sintering. HRTEM reveals a lattice spacing of 0.219 nm for the PtFe-S/MCS clusters, assignable to the PtFe (111) plane [Figure 5C]. HAADF-STEM and EDS mapping further reveal the homogeneous distribution and co-localization of Pt and Fe, together with dispersed S species throughout the carbon nanosphere, supporting the formation of sulfur-stabilized PtFe alloy clusters [Figure 5D]. PtCu-S/MCS also retains the mesoporous spherical morphology, but the metal species grow into larger nanoparticles with an average size of 5.6 ± 1.9 nm [Figure 5E and F], which can be attributed to the intrinsically higher aggregation tendency of Cu species during thermal treatment. The resolved lattice spacing of 0.221 nm can be indexed to the PtCu (111) plane, confirming alloy formation with a contracted Pt lattice [Figure 5G]. Elemental mapping shows broadly distributed Pt, Cu, C, and S signals across the nanosphere, indicating that sulfur anchoring remains effective at dispersing PtCu species [Figure 5H].

The elemental contents of the catalysts were further determined by Inductively Coupled Plasma - Optical Emission Spectroscopy (ICP-OES) and EDS analyses, and the results are summarized in Table 1. The Pt contents of PtCo-S/MCS, PtCu-S/MCS, PtFe-S/MCS, and PtCo/MCS were 5.1, 4.9, 5.0, and 4.8 wt.%, respectively, while the corresponding contents of Co, Cu, and Fe were close to the nominal values. Sulfur was detected only in the sulfur-containing catalysts, with contents ranging from 0.8 to 1.3 wt.%.

To further investigate the chemical states of Pt, Co, and S, X-ray photoelectron spectroscopy (XPS) measurements were performed. The Pt 4f spectra of all samples can be deconvoluted into metallic Pt^0 and partially oxidized Pt^{2+} species[36] [Figure 6A-C], the dominant Pt^0 contribution indicates the effective reduction of Pt precursors during H_2/Ar annealing, whereas the residual Pt^{2+} component is likely associated with electron-deficient Pt species at the alloy/support interface or Pt species interacting with sulfur-containing groups. The Co 2p, Fe 2p, and Cu 2p spectra reveal mixed surface valence states of the secondary metals [Figure 6D-F]. For PtCo-S/MCS, the Co 2p region consists of Co^{2+}/Co^{3+} components accompanied by satellite features[37]. PtFe-S/MCS exhibits Fe^0, Fe^{2+}, and Fe^{3+} contributions, while PtCu-S/MCS shows reduced Cu species together with Cu^{2+} related components and satellite peaks[38-40]. These partially oxidized surface species can be attributed to the high fraction of exposed metal atoms and the high surface energy of ultrasmall nanoparticles, which render their surfaces more susceptible to mild oxidation upon air exposure. Next, the S 2p spectra provide direct evidence for sulfur incorporation and metal-sulfur coordination [Figure 6G-I]. The low binding energy can be assigned to metal-sulfur bonds, including Co-S, Fe-S, and Cu-S, whereas the C-S-C contribution indicates the incorporation of sulfur species into the carbon framework[41]. The coexistence of M-S and C-S-C species suggests that sulfur serves as an interfacial anchoring motif, coupling the metal domains with the carbon support and thereby stabilizing highly dispersed bimetallic clusters or nanoparticles during high-temperature annealing, which differs from the classical strong metal-support interaction generally observed for reducible oxide-supported metal catalysts.

Based on the above structural characterizations, the role of sulfur anchoring can be further understood. During the impregnation process, sulfur species introduced by STG coordinate with Pt precursors and subsequently serve as anchoring sites during high-temperature annealing. The resulting metal-S interactions

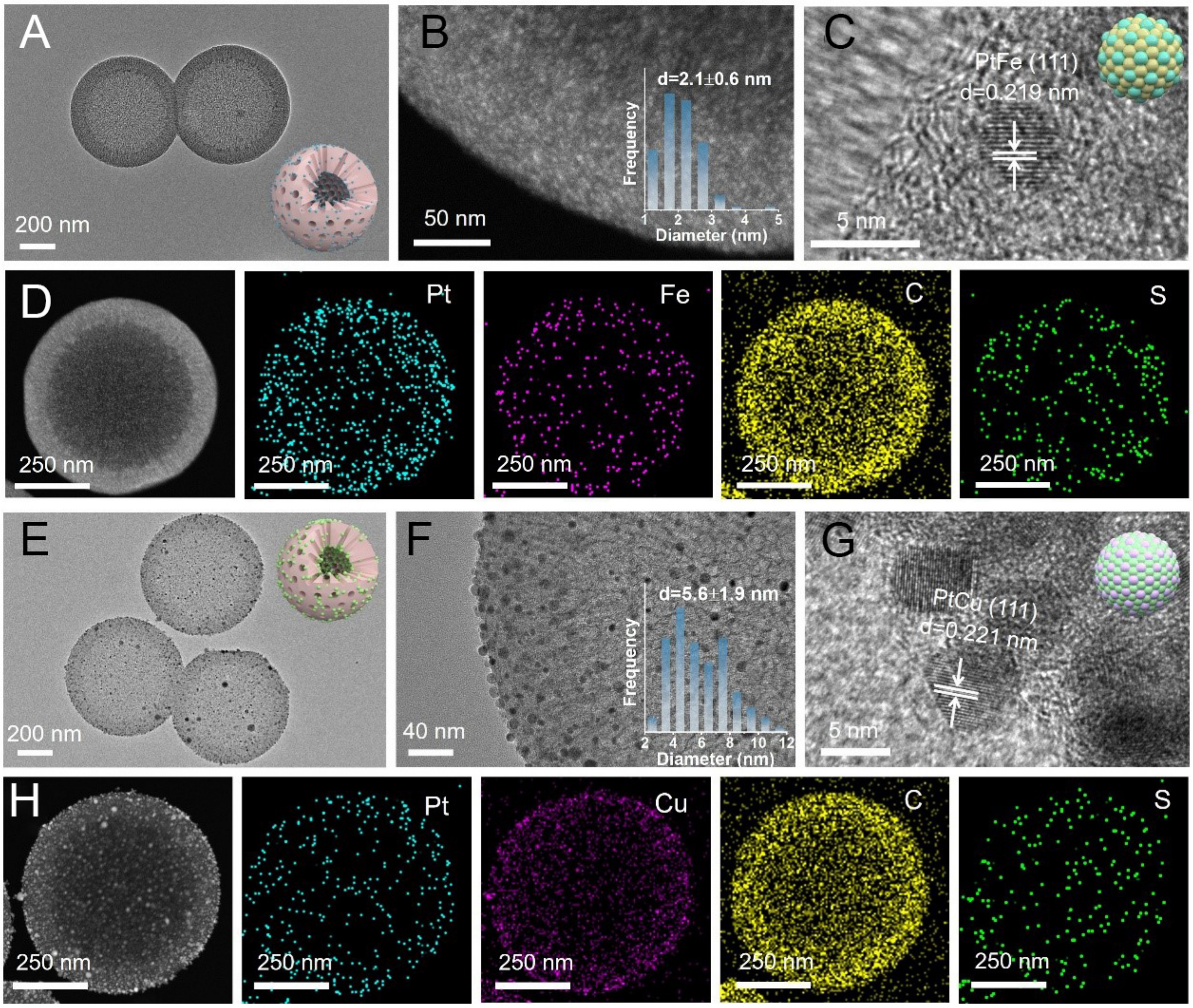

Figure 5. Microscopic characterization of PtFe–S/MCS and PtCu–S/MCS. (A) TEM image; (B) HAADF-STEM image with the inset showing the size distribution of metal clusters; and (C) HRTEM image; (D) HAADF-STEM image and the corresponding EDS elemental mappings of PtFe–S/MCS; (E and F) TEM images with the inset showing the size distribution of metal clusters; and (G) HRTEM image, (H) HAADF-STEM image and the corresponding EDS elemental mappings of PtCu–S/MCS. MCS: Mesoporous carbon nanospheres; HAADF-STEM: high-angle annular dark-field scanning transmission electron microscopy; HRTEM: high resolution transmission electron microscopy; EDS: energy-dispersive X-ray spectroscopy; TEM: transmission electron microscopy.

Table 1. Elemental content of various catalysts

Entry	Catalysts	Pt content[a] (wt.%)	Co/Cu/Fe content (wt.%)	S content[b] (wt.%)
1	PtCo-S/MCS	5.1	5.2	0.8
2	PtCu-S/MCS	4.9	5.1	0.9
3	PtFe-S/MCS	5.0	5.3	1.3
4	PtCo/MCS	4.8	5.5	0
5	Used PtCo-S/MCS	3.6	3.9	0.5

[a]The content was determined by ICP-OES; [b]The content was determined by EDS. MCS: Mesoporous carbon nanospheres; ICP-OES: Inductively Coupled Plasma - Optical Emission Spectroscopy; EDS: energy-dispersive X-ray spectroscopy.

suppress the migration and aggregation of metal species, leading to the formation of highly dispersed PtCo alloy clusters within the MCS framework. Compared with the sulfur-free PtCo/MCS catalyst, the smaller and more uniformly distributed PtCo alloy clusters provide a larger number of accessible active sites, which is

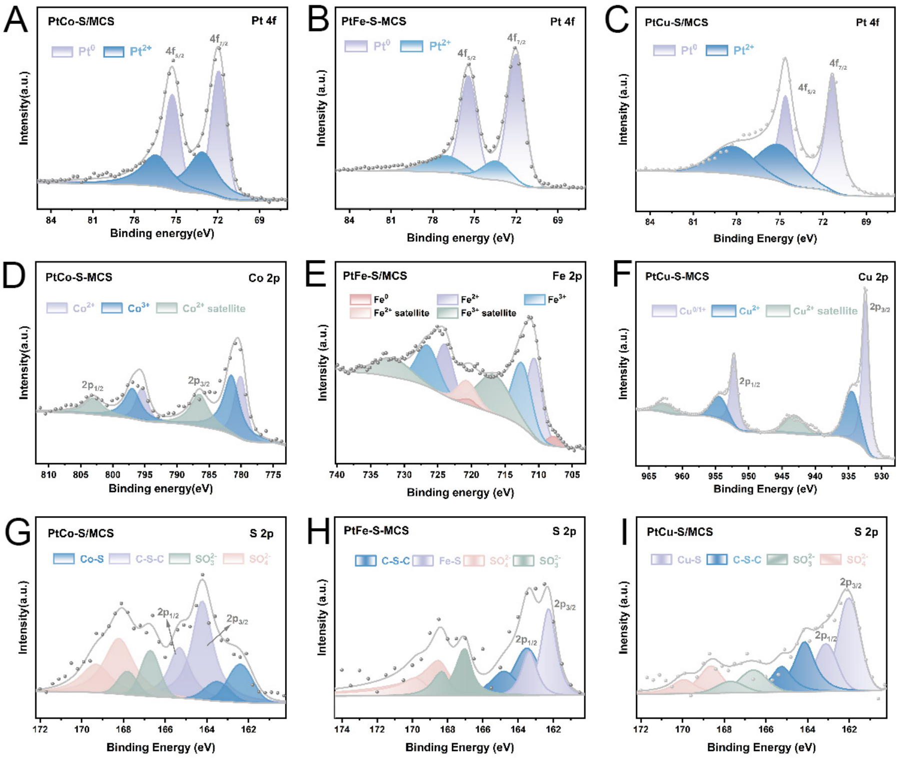

Figure 6. High-resolution XPS spectra of (A-C) Pt 4f for PtCo–S/MCS, PtFe–S/MCS and PtCu–S/MCS catalysts; (D) Co 2p for PtCo–S/MCS, (E) Fe 2p for PtFe–S/MCS, (F) Cu 2p for PtCu–S/MCS; (G-I) S 2p for PtCo–S/MCS, PtFe–S/MCS and PtCu–S/MCS catalysts. MCS: Mesoporous carbon nanospheres; XPS: X-ray photoelectron spectroscopy.

beneficial for the transfer hydrogenation of FFA to FOL.

To further investigate the role of sulfur, a post-sulfurized catalyst (PtCo-S/MCS) was prepared by introducing sulfur species onto preformed PtCo/MCS using thiourea. As shown in Supplementary Figure 1, sulfur was successfully introduced into the catalyst, as confirmed by elemental mapping. However, PtCo-S/MCS exhibited a much larger average particle size (23.2 ± 6.6 nm) than PtCo-S/MCS (2.1 ± 0.5 nm) [Supplementary Figure 2]. These results suggest that sulfur introduced after catalyst formation cannot reproduce the dispersion-promoting effect observed in PtCo-S/MCS.

Catalytic performance

The catalytic performance of the as-prepared catalysts was evaluated in the selective transfer hydrogenation of FFA using IPA as both solvent and hydrogen donor. As shown in Figure 7A, pure MCS mainly affords acetal formation with negligible furfuryl alcohol (FOL) production, indicating that the carbon support itself lacks effective hydrogenation capability. Among the bimetallic catalysts, PtCo-S/MCS exhibits the most favorable catalytic performance, affording a FOL yield of 98.9%. In contrast, PtCu-S/MCS exhibits a much lower FOL yield of 62.3%, which can be attributed to the different regulatory effect of Cu on the catalytic behavior as well as the larger size of the PtCu alloy particles. However, despite having a particle size comparable to that of PtCo-S/MCS, PtFe-S/MCS exhibits a significantly lower catalytic performance, affording only an 8.2% FOL yield, which suggests that the catalytic performance is strongly influenced by the electronic interaction between Pt and the secondary metal. Compared with Co, Fe may induce a less favorable adsorption and activation environment for FFA transfer hydrogenation, leading to the substantially lower FOL yield observed for PtFe-S/MCS. The formation of acetal is likely associated with the reaction between FFA and IPA under the reaction conditions. In the absence of efficient hydrogenation sites, acetal

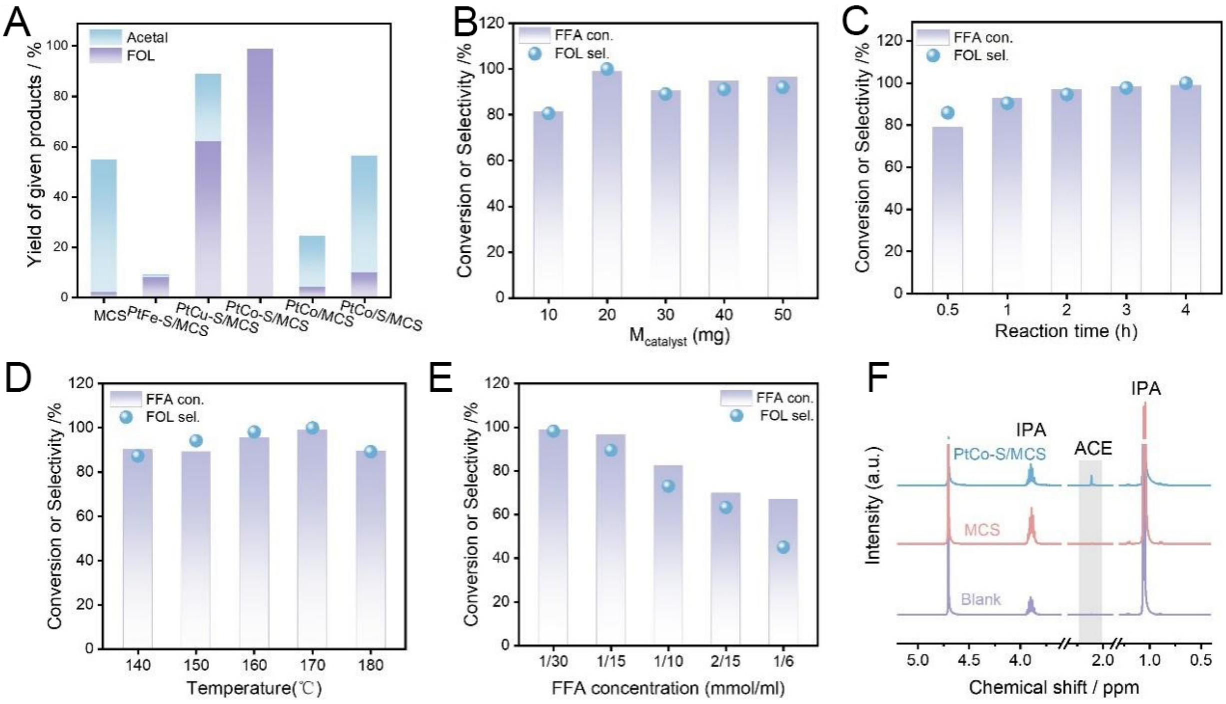

Figure 7. (A) Product distribution across different catalysts; Reaction conditions: 20 mg of catalyst, 0.5 mmol of FFA, 15 mL of IPA, 170 °C, 4 h, 900 rpm; Effects of (B) catalyst amount; (C) reaction time (Each reaction time point was obtained from an independent experiment); (D) reaction temperature; and (E) (FFA concentration on catalytic performance over PtCo-S/MCS; Reaction conditions: 10-50 mg of catalyst, 0.5-2.5 mmol of FFA, 15 mL of IPA, 140-180 °C, 0.5-4 h, 900 rpm; (F) ^{1}H NMR spectra of the reaction solutions obtained from blank, MCS, and PtCo-S/MCS systems; Reaction conditions: 20 mg of catalyst, 15 mL of IPA, 170 °C, 4 h, 900 rpm. FOL: Furfuryl alcohol; FFA: furfural; IPA: isopropanol; ACE: acetone; MCS: mesoporous carbon nanospheres; NMR: nuclear magnetic resonance.

tends to accumulate as a major product. By contrast, the highly dispersed PtCo alloy clusters facilitate hydrogen transfer and carbonyl hydrogenation, thereby promoting FOL formation and suppressing acetal accumulation. Notably, the sulfur-free PtCo/MCS shows markedly inferior activity accompanied by pronounced acetal formation, underscoring the importance of sulfur-assisted metal anchoring in steering both activity and selectivity.

The reaction parameters were further optimized using PtCo-S/MCS as the main catalyst. As shown in Figure 7B, increasing the catalyst dosage from 10 to 20 mg markedly enhances both FFA conversion and FOL selectivity, reaching 98.9%. Further increasing the catalyst amount does not provide additional improvement, indicating that 20 mg is sufficient to drive the reaction efficiently under the present conditions. Figure 7C reveals a gradual increase in FFA conversion and FOL yield with prolonged reaction time. The FOL yield reached 98.9% after 4 h under the optimized reaction conditions. Temperature also plays a decisive role in regulating the reaction pathway. Raising the temperature from 140 to 170 °C [Figure 7D] progressively improved the catalytic performance, whereas a further increase to 180 °C leads to decreased FFA conversion and FOL selectivity, which is due to enhanced side reactions at elevated temperature. In addition, the initial FFA concentration strongly affects the reaction outcome. As shown in Figure 7E, diluted feeds favor high conversion and FOL selectivity, while increasing the substrate concentration results in a continuous decline in selectivity. The effect of different hydrogen donors on the transfer hydrogenation of FFA was further investigated, and the results are shown in Supplementary Figure 3. Among the alcohols examined, IPA exhibited the best performance, affording 98.9% FFA conversion and nearly 100% FOL selectivity. In contrast, ethanol resulted in lower FOL selectivity, while methanol and n-butanol showed intermediate performance, which indicates that IPA is the most suitable hydrogen donor for the present catalytic system. Thus, the optimized reaction conditions were identified as follows: 20 mg of catalyst, IPA as the hydrogen

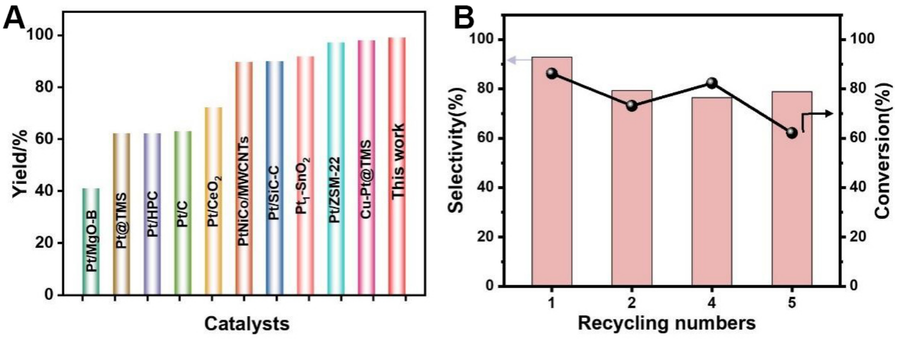

Figure 8. (A) Comparison of the FOL yield achieved by PtCo-S/MCS with reported Pt-based catalysts[17,42-49]; (B) Recycling performance of PtCo-S/MCS for the transfer hydrogenation of FFA to FOL. Reaction conditions: 20 mg of catalyst, 0.5 mmol of FFA, 15 mL of IPA, 170 °C, 4 h, 900 rpm. TMS: TS-1 zeolite@mesoporous silica core–shell structure; HPC: hierarchical porous carbon; FOL: furfuryl alcohol; MCS: mesoporous carbon nanospheres; FFA: furfural; IPA: isopropanol.

donor, 0.5 mmol of FFA, 170 °C, and 4 h. The hydrogenation of a series of carbonyl-containing compounds was also investigated to evaluate the applicability of the PtCo-S/MCS catalyst. As shown in Supplementary Table 1, selectivities toward the corresponding alcohol products above 85% were achieved in all cases, indicating the potential applicability of PtCo-S/MCS in the catalytic upgrading of biomass-derived carbonyl compounds.

To verify the role of IPA in the transfer hydrogenation process, a control experiment in the absence of FFA was performed, and the liquid-phase products were analyzed by ^{1}H NMR after reaction. As shown in Figure 7F, the PtCo-S/MCS-catalyzed system displays a clear acetone (ACE) signal, which is absent or much weaker in the blank and MCS control experiments. Since ACE is the dehydrogenation product of IPA, this result confirms that IPA serves as the hydrogen donor and participates directly in the catalytic transfer hydrogenation of FFA. Together, the catalytic tests and NMR analysis establish PtCo-S/MCS as an efficient catalyst for the selective conversion of FFA to FOL, with its superior performance arising from highly dispersed, sulfur-stabilized PtCo alloy clusters that promote coupled IPA dehydrogenation and FFA hydrogenation.

To further evaluate catalytic performance, the yield of FOL compared with reported Pt-based catalysts [Figure 8A]. PtCo-S/MCS achieves a FOL yield of 98.9%, outperforming most reported Pt-based catalysts. Next, the recyclability of PtCo-S/MCS was further evaluated under the optimized reaction conditions. As shown in Figure 8, the catalyst maintains a relatively high FOL selectivity over repeated runs, indicating that the dominant reaction pathway toward selective C=O hydrogenation is largely preserved during recycling. Although the furfural conversion gradually decreases with successive cycles, PtCo-S/MCS still retains appreciable catalytic activity after five runs. This result suggests that the sulfur-anchored PtCo alloy clusters possess reasonable operational stability, while the observed activity loss may be attributable to partial surface blocking or unavoidable catalyst loss during recovery and reuse. Overall, the recycling test supports the structural robustness of the sulfur-confined catalyst and its ability to sustain selective furfural hydrogenation under repeated reaction conditions.

To further investigate the reason for the decline in catalyst performance, TEM and N_2 adsorption-desorption analysis of the used PtCo-S/MCS catalyst were performed. As shown in Figure 9A and B, the MCS support was slightly damaged, with PtCo alloy clusters distributed within it at an average size of 2.6 nm, which is slightly larger compared to the 2.1 nm of the fresh catalyst. Combined with the HAADF-STEM result showing that sulfur remains uniformly distributed, this further demonstrates the robust anchoring effect of

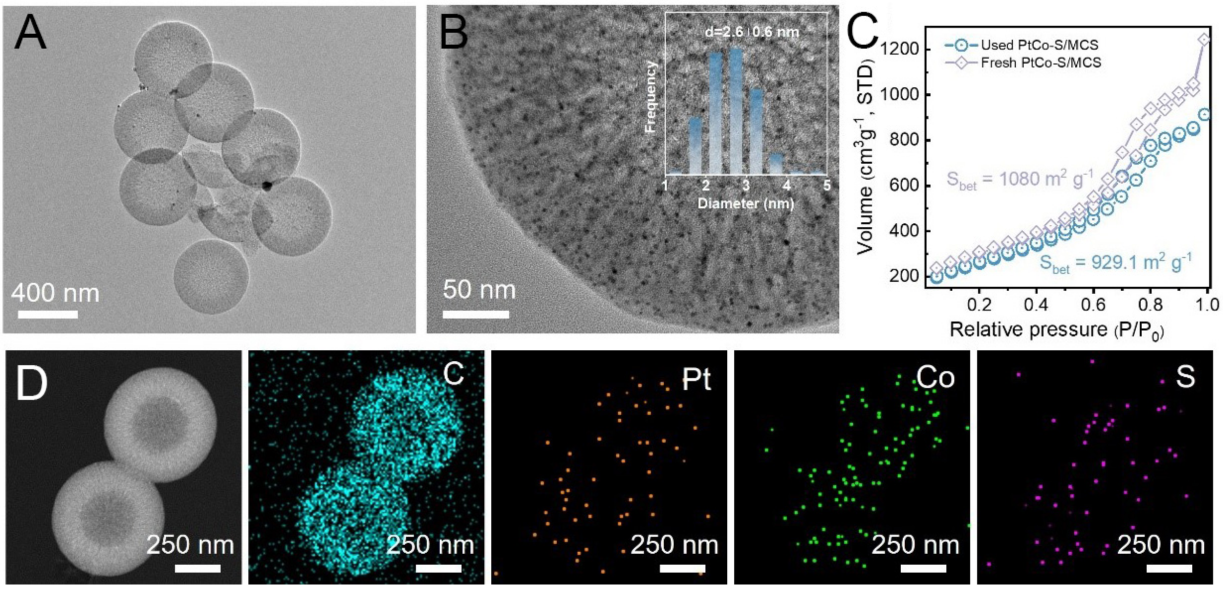

Figure 9. Characterization of the used PtCo–S/MCS catalyst. (A and B) TEM images with the inset showing the size distribution of metal clusters; (C) N_2 adsorption-desorption isotherm (the inset shows pore size distribution curve); (D) HAADF-STEM image and the corresponding EDS elemental mappings. STD: Standard temperature and pressure; MCS: mesoporous carbon nanospheres; TEM: transmission electron microscopy; HAADF-STEM: high-angle annular dark-field scanning transmission electron microscopy; EDS: energy-dispersive X-ray spectroscopy.

sulfur on the metal [Figure 9C]. Moreover, the N_2 adsorption-desorption isotherm still exhibits a typical Type IV curve [Figure 9D], with the specific surface area of PtCo-S/MCS decreased from 1,080 to 929 m^2 g^{-1} after recycling, which may be attributed to the partial blockage of the porous structure of the catalyst during the high-temperature reaction process. Furthermore, as determined by ICP-OES, the Pt and Co contents after the reaction decreased from their initial values of 5.1% and 5.2% to 3.6% and 3.9%, respectively [Table 1]. Therefore, the detachment of S-containing PtCo alloy clusters from the MCS support, along with the partial blockage of the mesoporous structure, are the primary reasons for the performance degradation of the catalyst during cycling. Future work should focus on strengthening the bonding between sulfur and the MCS support.

CONCLUSION

In summary, a sulfur-anchored mesoporous carbon nanosphere strategy was developed to stabilize Pt-based bimetallic alloy clusters under high-temperature reductive annealing. The mesoporous carbon framework provides spatial confinement and mass-transport channels, while sulfur-containing sites serve as interfacial anchors that suppress metal migration and promote uniform alloy formation. As a result, PtCo-S/MCS exhibits highly dispersed PtCo alloy clusters with an average size of 2.1 nm, in sharp contrast to the aggregated and compositionally heterogeneous nanoparticles formed without sulfur anchoring. The strategy is also applicable to PtFe and PtCu systems. In FFA transfer hydrogenation, PtCo-S/MCS achieves a FOL yield of 98.9% and maintains favorable catalytic performance during recycling. This work highlights sulfur-mediated interfacial anchoring as an effective route to thermally stable bimetallic nanocatalysts for selective biomass upgrading.

DECLARATIONS

Authors' contributions

Writing-original draft: Gao, B.
Writing-review & editing: Gao, B.; Wang, L.; Jiang, W.; Qiu, P.
Validation: Gao, B.; Luo, Y.
Methodology: Gao, B.

Investigation: Gao, B.
Formal analysis: Gao, B.; Luo, Y.; Yu, X.
Conceptualization: Gao, B.; Qiu, P.
Resources: Luo, Y.; Qiu, P.
Data curation: Luo, Y.; Yu, X.
Supervision: Wang, L.; Qiu, P.; Luo, W.
Project administration: Qiu, P.; Luo, W.
Funding acquisition: Qiu, P.; Luo, W.

Availability of data and materials

All experimental methods and key results are fully described in the manuscript to ensure reproducibility of the work. Any additional relevant information can be obtained from the corresponding authors upon reasonable request.

AI and AI-assisted tools statement

Not applicable

Financial support and sponsorship

This work was supported by the National Natural Science Foundation of China (52225204, 52173233, and 52202085), the Innovation Program of Shanghai Municipal Education Commission (2021-01-07-00-03-E00109), Natural Science Foundation of Shanghai (23ZR1479200), "Shuguang Program" Supported by the Shanghai Education Development Foundation and Shanghai Municipal Education Commission (20SG33), the Fundamental Research Funds for the Central Universities (2232024Y-01) and the DHU Distinguished Young Professor Program (LZA2022001 and LZB2023002).

Conflicts of interest

Qiu, P. is a Senior Editorial Board Member of the journal *Micro Nano Science*. Qiu, P. was not involved in any steps of editorial processing, notably including reviewers' selection, manuscript handling and decision making. The other authors declare that there are no conflicts of interest. Luo, W. is an Associate Editor of the journal *Micro Nano Science*. Luo, W. was not involved in any steps of editorial processing, notably including reviewers' selection, manuscript handling and decision making. The other authors declare that there are no conflicts of interest.

Ethical approval and consent to participate

Not applicable

Consent for publication

Not applicable

Copyright

Supplementary Materials

Supplementary Materials

REFERENCES

1. An, Z.; Yang, P.; Duan, D.; et al. Highly active, ultra-low loading single-atom iron catalysts for catalytic transfer hydrogenation. *Nat. Commun.* **2023**, *14*, 6666. DOI PubMed PMC
2. Zhang, Y.; Zhang, G.; Hou, Q.; et al. Pt-Co single-atom alloy toward furfural hydrogenation-rearrangement tandem reaction in the aqueous phase. *ACS. Catal.* **2025**, *15*, 1206-16. DOI
3. Yao, W.; Chen, J.; Wang, Y.; et al. Nitrogen-doped carbon composites with ordered macropores and hollow walls. *Angew. Chem. Int. Ed.* **2021**, *60*, 23729-34. DOI

4. Li, X.; Jia, P.; Wang, T. Furfural: A promising platform compound for sustainable production of C_4 and C_5 chemicals. *ACS. Catal.* **2016**, *6*, 7621-40. DOI
5. Guo, T.; Luo, Y.; Li, H.; et al. Single nickel atoms anchored on porous N-doped nanocarbon with dual reaction sites for highly-efficient transfer hydrogenation of furfural to furfuryl alcohol. *Chem. Eng. J.* **2024**, *500*, 156659. DOI
6. Iroegbu, A. O. C.; Ray, S. S. On the chemistry of furfuryl alcohol polymerization: a review. *J. Polym. Sci.* **2023**, *62*, 1044-60. DOI
7. Cao, P.; Lin, L.; Qi, H.; et al. Zeolite-encapsulated cu nanoparticles for the selective hydrogenation of furfural to furfuryl alcohol. *ACS. Catal.* **2021**, *11*, 10246-56. DOI
8. Liang, W.; Xu, G.; Fu, Y. Accurate restricted transition-state shape selective hydrogenation of furfural over zeolite confined Cu catalyst. *Chin. J. Catal.* **2025**, *74*, 71-81. DOI
9. Bi, S.; Zhou, S.; Liu, T.; et al. Sub-2 Nm palladium phosphide: a highly active and selective catalyst for the hydrogenation of furfural to furfuryl alcohol. *Angew. Chem. Int. Ed.* **2025**, *64*, e202515805. DOI
10. Zhang, T.; Jing, Y.; Yu, Z.; et al. Catalytic mechanisms and systems of the conversion of furfural to γ-valerolactone via transfer hydrogenation pathway: a review. *Coord. Chem. Rev.* **2026**, *554*, 217615. DOI
11. Li, X.; Cao, J.; Chen, G.; et al. A radical-assisted approach to high-entropy alloy nanoparticle electrocatalysts under ambient conditions. *ACS. Nano.* **2025**, *19*, 7851-63. DOI
12. Wu, M.; Bai, L.; Deng, F.; He, J.; Song, K.; Li, H. Organic-inorganic hybrid materials for catalytic transfer hydrogenation of biomass-derived carbonyl-containing compounds. *Coord. Chem. Rev.* **2025**, *523*, 216259. DOI
13. Meng, Y.; Jian, Y.; Li, J.; et al. Surface-active site engineering: Synergy of photo- and supermolecular catalysis in hydrogen transfer enables biomass upgrading and H_2 evolution. *Chem. Eng. J.* **2023**, *452*, 139477. DOI
14. Wang, Y.; Cui, Q.; Guan, Y.; Wu, P. Facile synthesis of furfuryl ethyl ether in high yield *via* the reductive etherification of furfural in ethanol over Pd/C under mild conditions. *Green. Chem.* **2018**, *20*, 2110-7. DOI
15. Long, Y.; Wang, Y.; Wu, H.; Xue, T.; Wu, P.; Guan, Y. Doping Pd/SiO_2 with Na^+: changing the reductive etherification of C=O to furan ring hydrogenation of furfural in ethanol. *RSC. Adv.* **2019**, *9*, 25345-50. DOI
16. Zhao, M.; Wang, X.; Xu, J.; et al. Strengthening the metal-acid interactions by using CeO_2 as regulators of precisely placing Pt species in ZSM-5 for furfural hydrogenation. *Adv. Mater.* **2024**, *36*, 2313596. DOI
17. Li, X.; Wu, J.; Wang, X.; et al. Oxidation state of highly dispersed Pt subnanoclusters correlates with d-p orbital hybridization for 100% selectivity in furfural hydrogenation. *ACS. Catal.* **2026**, *16*, 3346-56. DOI
18. Wang, J.; Lin, H.; Chan, Q.; Zhao, Y.; He, X. Atomically dispersed Pt-Sn nanocluster catalysts for enhanced toluene hydrogenation in LOHC systems. *Colloids. Interfaces.* **2025**, *9*, 85. DOI
19. Fu, R.; Kong, Y.; Wang, G.; et al. Promoting the hydrogen spillover via dual active sites synergistically for efficient photo-driven nitrogen fixation. *Appl. Catal. B. Environ.* **2025**, *362*, 124671. DOI
20. Duan, X.; Fang, Y.; Ruan, L.; Deng, M.; Zhu, L. Furfural selective hydrogenation at low temperature: Enhancing catalytic performance via Pt-Co synergistic effect. *Int. J. Hydrogen. Energy.* **2026**, *197*, 152333. DOI
21. Zhao, Z.; Li, X.; Liu, X.; et al. Pt/Fe-TiO_2-catalyzed selective carbonyl hydrogenation: Fe-promoted hydrogen spillover. *ACS. Catal.* **2024**, *14*, 4478-88. DOI
22. Taylor, M. J.; Beaumont, S. K.; Islam, M. J.; et al. Atom efficient PtCu bimetallic catalysts and ultra dilute alloys for the selective hydrogenation of furfural. *Appl. Catal. B-Environ.* **2021**, *284*, 119737. DOI
23. Xiao, A.; Xu, H.; Cui, H.; Cheng, Z.; Zhou, Z. Bimetallic and trimetallic Pt-based catalysts for selective hydrogenation of p-chloronitrobenzene to p-chloroaniline. *Appl. Catal. A-Gen.* **2023**, *666*, 119424. DOI
24. Jin, Y.; Wang, P.; Mao, X.; et al. A topdown strategy to realize surface reconstruction of small-sized platinum-based nanoparticles for selective hydrogenation. *Angew. Chem. Int. Ed.* **2021**, *60*, 17430-4. DOI
25. Shao, R.; Xu, X.; Zhou, Z.; et al. Promoting ordering degree of intermetallic fuel cell catalysts by low-melting-point metal doping. *Nat. Commun.* **2023**, *14*, 5896. DOI PubMed PMC
26. Jing, L.; Wang, W.; Tian, Q.; et al. Efficient Neutral H_2O_2 electrosynthesis from favorable reaction microenvironments via porous carbon carrier engineering. *Angew. Chem. Int. Ed.* **2024**, *63*, e202403023. DOI
27. Wang, Y.; Yao, Y.; Xu, C.; et al. A universal solid-phase synthetic strategy for ultrafine intermetallic libraries confined in ordered mesoporous carbon. *Adv. Mater.* **2024**, *37*, 2416111. DOI
28. Qi, C.; Bao, W.; Xu, J.; et al. Integrated two-in-one strategy for efficient neutral hydrogen peroxide electrosynthesis via phosphorous doping in 2D mesoporous carbon Carriers. *Angew. Chem. Int. Ed.* **2025**, *64*, e202500177. DOI
29. Tian, Z.; Wang, W.; Dong, C.; Deng, X.; Wang, G. A general and scalable approach to sulfur-doped Mono-/Bi-/trimetallic nanoparticles confined in mesoporous carbon. *ACS. Nano.* **2023**, *17*, 3889-900. DOI

30. Luo, Z.; Qiao, Y.; Tang, R.; et al. Seaweed-derived hierarchical porous carbon for high-rate performance supercapacitors. *New. J. Chem.* **2026**, *50*, 3294-305. DOI
31. Wassner, M.; Eckardt, M.; Reyer, A.; et al. Synthesis of amorphous and graphitized porous nitrogen-doped carbon spheres as oxygen reduction reaction catalysts. *Beilstein. J. Nanotechnol.* **2020**, *11*, 1-15. DOI PubMed PMC
32. Zheng, Z.; Liu, B.; Qiu, J.; et al. Effectively regulating electrooxidation of formic acid over bimetallic PtCo alloys via the integration of theory and experiment. *ACS. Catal.* **2024**, *14*, 18333-44. DOI
33. Cao, Z.; Dong, F.; Pan, J.; Xia, W.; Hu, J.; Xu, X. Heteroatomic platinum-cobalt synergetic active centers with charge polarization enable superior hydrogen evolution performance in both acid and base media. *ACS. Appl. Energy. Mater.* **2022**, *5*, 1496-504. DOI
34. Huang, J.; Peng, B.; Stracensky, T.; et al. 1D PtCo nanowires as catalysts for PEMFCs with low Pt loading. *Sci. China. Mater.* **2021**, *65*, 704-11. DOI
35. Shen, J.; Hu, S.; Tian, N.; et al. P-doping strategy increasing the durability of PtCo nanoparticles for the oxygen reduction reaction. *ACS. Sustainable. Chem. Eng.* **2023**, *11*, 11660-7. DOI
36. Xie, M.; Zhu, G.; Yang, H.; et al. Periodic adjacent Pd-Fe pair sites for enhanced nitrate electroreduction to ammonia via accelerating proton relay. *Adv. Energy. Mater.* **2024**, *14*, 2401717. DOI
37. Zhang, X. Y.; Yin, H.; Liu, H. H.; et al. Decoupling adsorption of key intermediates enabled by asymmetric 3d-5d-orbital hybridization: durable high-performance AEM water electrolysis and Zn-air batteries. *Angew. Chem. Int. Ed.* **2026**, *65*, e24805. DOI
38. Gao, B.; Zhang, J.; Zhang, M.; Li, H.; Yang, J. Highly dispersed PdCu supported on MCM-41 for efficiently selective transfer hydrogenation of furfural into furfuryl alcohol. *Appl. Surf. Sci.* **2023**, *619*, 156716. DOI
39. Liu, F.; Wang, X.; Wu, J.; et al. A novel homogeneous amphipathic PTFE/β-FeOOH nanofiber membrane for emulsion separation and photocatalytic degradation in harsh environments. *Adv. Membr.* **2026**, *6*, 100187. DOI
40. Yin, S.; Yan, Y.; Chen, L.; et al. FeN_4 active sites electronically coupled with PtFe alloys for ultralow Pt loading hybrid electrocatalysts in proton exchange membrane fuel cells. *ACS. Nano.* **2023**, *18*, 551-9. DOI
41. Yin, P.; Yan, Q. Q.; Liang, H. W. Strong metal-support interactions through sulfur-anchoring of metal catalysts on carbon supports. *Angew. Chem. Int. Ed.* **2023**, *62*, e202302819. DOI
42. Fu, M.; Shan, Z.; Zhang, M.; et al. Pt Nanoparticles on $Mg(OH)_2$ for the selective hydrogenation of furfural to furfuryl alcohol. *ACS. Appl. Nano. Mater.* **2025**, *8*, 11002-14. DOI
43. Wang, S.; Lv, Y.; Ren, J.; et al. Ultrahigh selective hydrogenation of furfural enabled by modularizing hydrogen dissociation and substrate activation. *ACS. Catal.* **2023**, *13*, 8720-30. DOI
44. Byun, M. Y.; Lee, M. S. Pt supported on hierarchical porous carbon for furfural hydrogenation. *J. Ind. Eng. Chem.* **2021**, *104*, 406-15. DOI
45. Byun, M. Y.; Lee, M. S. Effect of carboxylate stabilizers on the performance of Pt/C catalysts for furfural hydrogenation. *J. Environ. Chem. Eng.* **2021**, *9*, 106293. DOI
46. Ruan, L.; Zhu, L.; Zhang, X.; et al. A highly efficient, selective and stable PtCoNi/MWCNTs nanocatalyst for furfural hydrogenation to furfuryl alcohol under mild reaction conditions. *Fuel* **2023**, *333*, 126222. DOI
47. Wang, G.; Yao, R.; Xin, H.; Guan, Y.; Wu, P.; Li, X. At room temperature in water: efficient hydrogenation of furfural to furfuryl alcohol with a Pt/SiC-C catalyst. *RSC. Adv.* **2018**, *8*, 37243-53. DOI
48. Wang, Y.; Wang, Z.; Xu, C.; Zhou, S. Synthesis of alumina supported Pt-SnO_2 hybrid nanostructures by *in situ* transformation of PtSn alloy nanoparticles and their application as highly efficient catalysts for selective hydrogenation of furfural. *J. Phys. Chem. C.* **2023**, *127*, 4033-41. DOI
49. Wang, X.; Wang, C.; Bi, W.; Qu, W.; Tian, Z. Ligand-protected and lowered-temperature hydrothermal synthesis of platinum encapsulated in TON zeolite for shape-selective hydrogenation of furfural to furfuryl alcohol. *J. Mater. Chem. A.* **2025**, *13*, 289-304. DOI